Electron-spin diffusion in proton-irradiation microstructured (fluoranthene)$_2$PF$_6$

T. Wokrina
Physikalisches Institut, Universität Karlsruhe, D-76128 Karlsruhe, Germany

J. Gmeiner
Bayreuther Institut für Makromolekülforschung, Universität Bayreuth, D-95440 Bayreuth, Germany

N. Kaplan* and E. Dormann
Physikalisches Institut, Universität Karlsruhe, D-76128 Karlsruhe, Germany

(Received 8 November 2002; published 18 February 2003)

The properties of the quasi-one-dimensional organic conductor (fluoranthene)$_2$PF$_6$ are modified by proton irradiation ($E_p = 25$ MeV, $n_p = 5.4 \times 10^{16}$ cm^{-2}). The crystals are characterized by measurement of static magnetic susceptibility, cw–electron spin resonance, static magnetic-field gradient pulsed electron spin resonance and especially by one- and two-dimensional electron-spin-resonance imaging. Electron-spin diffusion constant parallel to the stacking direction is reduced by one order of magnitude, whereas the perpendicular direction remains essentially unchanged, for homogeneous proton irradiation. A well-defined periodic 100-μm structure is impressed using appropriate metal grids in the proton beam. Thus the diffusion constant, as well as the concentration of localized defects, is spatially modulated. Experimental evidence of the coherence phenomena of the diffusing electron spins moving between the artificially created reflecting walls is presented.

DOI: 10.1103/PhysRevB.67.054103 PACS number(s): 61.72.−y, 61.80.Jh, 72.15.Lh, 76.30.Pk

I. INTRODUCTION

The dynamic properties of electrons in the so-called one-dimensional organic metals are known to be sensitive to interruptions occurring along the conduction chains or molecular stacks. Many such systems have been reported already, and the crystalline (fluoranthene)$_2 M$F$_6$ (M = As, P, Sb) family may be considered as a representative example. It is thus tempting to try and microstructure these properties by creating in the crystal, in a controlled manner, geometrically patterned barriers perpendicular to the preferred direction of conduction. Such barriers would block the free motion of the spins and charge carriers along the conducting channels. Being mechanically and environmentally delicate, candidate one-dimensional (1D) organic metal single-crystal samples are not very amenable to direct mechanical imposition of structured barriers. However, it is possible to create such barriers using radiation damage techniques. Indeed, as will be detailed in Sec. III, a radiation damage induced by a proton beam could be utilized to generate patterned barriers in a single-crystal sample of (fluoranthene)$_2$PF$_6$. To use the data acquired from the microstructured sample in an optimal manner, it is of course desirable to investigate also the *spatial distribution* of the investigated properties. Such spatial mapping is attainable using appropriate electron-spin-resonance (ESR) imaging schemes.

Motivated by the above reasoning, and utilizing the outlined ''building blocks,'' namely, microstructured barrier pattern and some ESR imaging procedures, the present study focuses on the influence of microstructured barriers on major parameters characterizing the electrons in the ''metallic'' phase of a (fluoranthene)$_2$PF$_6$ [(FA)$_2$PF$_6$] sample, namely, electron self-diffusion, local electron density, and electronic relaxation.

The paper is organized as follows. Essential background is reviewed shortly in Sec. II. Preparatory experimental details (crystal growth, proton irradiations, magnetic characterizations, pulsed ESR procedures) are described in Sec. III. In Sec. IV we present the experimental results. These consist of 1D projections and 2D projection-reconstruction images aiming at revealing the spatial distribution of relaxation times (T_2), electron spin susceptibilities, and diffusion constants along the length of homogeneously irradiated or microstructured (FA)$_2$PF$_6$ crystals. The results are discussed in Sec. V, and the main conclusions are summarized in Sec. VI.

II. BACKGROUND

Figure 1 illustrates schematically our current picture of real quasi-one-dimensional conductors such as the arene radical cation salts. These are built from one-dimensional stacks of aromatic hydrocarbon (i.e., arene) molecules—the so-called conducting chains—with octahedral anion complexes, such as hexafluorophosphate, in between the stacks.[1] The scattering time for conduction electron motion parallel to the stacking direction, $\tau_\parallel$, ranges between 10^{-15} s and 10^{-14} s at room temperature, and is thus much shorter than the perpendicular hopping time, $\tau_\perp$, ranging from about 10^{-12} s up to 10^{-10} s. The anisotropy of the macroscopic

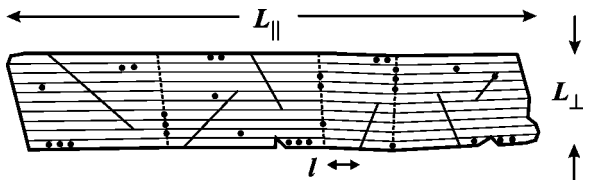

FIG. 1. Schematic view of a ''real'' quasi-one-dimensionally conducting arene radical cation salt crystal. External dimensions ($L_\parallel, L_\perp$) and an individual channel length of free diffusive motion (l) are indicated. Grain boundaries (broken lines), cracks (solid lines), and localized defects (dots) are symbolized as the typical interruptions of the extended one-dimensional channels.

microwave electrical conductivity varies in the range of $\sigma_{\|}/\sigma_{\perp}=10^3 \ldots 10^4$, but is mostly influenced by defects and mosaic structure. Some samples were observed with regions in which individual channels allow for the unrestricted diffusive motion of the conduction electron spin from one end of the crystal to the other.[2] However, usually there are many defects in the arene radical cation salts—depending on the general composition and the individual growth conditions, between 10^{-5} and 10^{-2} Curie-like paramagnetic defects per formula unit have been reported. Furthermore, extended obstacles such as cracks and grain boundaries of mosaiclike microstructures exist which cannot be bypassed by the slow perpendicular hopping motion during short time intervals of the order of $\tau_{\perp}$. These extended obstacles are considered as one of the causes for the monotonic increase of the absolute value of the electrical conductivity $\sigma_{\|}$ between dc (direct current) up to optical frequencies.

Maresch and Mehring[3–5] have pioneered the study of the anisotropic motion of the charge and spin carriers in quasi-one-dimensional conductors by combining the pulsed ESR (Ref. 6) with application of magnetic-field gradients. For a FA radical cation salt they demonstrated that the techniques known from nuclear magnetic resonance for the measurement of diffusion constants D (Refs. 7 and 8) can be adopted for the derivation of the electronic $D(\theta)$. The quantitative analysis of $D(\theta)$ yields especially accurate values of $D_{\|}$ and $D_{\perp}$.[5] The application of pulsed magnetic-field gradients in the spin-echo sequence allows the clear differentiation between relaxation and diffusion of the spins.[2,3,9] Restrictions to the free diffusive motion as pictured in Fig. 1 thus can be distinguished from the contribution of localized spins.[2,9,10] Three-dimensional spatial resolution of these properties was recently achieved as well.[2,11,12] Furthermore, for a perylene radical cation salt the correspondence of the charge motion with the spin motion along the conduction chains was verified by comparison of their temperature dependence.[13] Nevertheless, we continue to use the term ''diffusion constant D'' rather than ''self-diffusion coefficient D'' in the following, because it is *a priori* not clear if the diffusive motions of electron spins and electric charges are equivalent for motion parallel as well as perpendicular to the arene radical cation stacks. The restriction to free diffusive motion of the conduction electron spins in arene radical cation salts can be monitored also by static magnetic-field gradient spin-echo ESR (SGSE).[10] The anisotropy of spin relaxation (T_2), spin diffusion constant $[D(\theta)]$, and the average lengths of the channels available for the free diffusive motion, $\overline{l_{\|}}$ and $\overline{l_{\perp}}$, are thus accessible.[14,15] The similarity of the $\overline{l_{\|}}$ values for various arene radical cation salts, ranging between 50 and 100 μm, is a rather puzzling result of the SGSE analysis.[16] The more pronounced sample dependence of the absolute values of $D_{\|}$ seems to reflect the defect distribution of individual single crystals with better sensitivity. In fact, this state of affairs is precisely what prompted the investigation of deliberately microstructured single crystals of $(FA)_2PF_6$ reported below. The well-defined geometrical barrier structure was imposed on the conducting stacks using irradiation with high-energy protons.

TABLE I. Sample dimensions and characteristics.

Sample	$L_{\|}$ (mm)	$L_{\perp}$ (mm)	Age (yr)	Treatment
A	2.35	0.375, 0.350	<1	Homogeneous irradiation
B	1.575	0.550, 0.575	<1	Microstructured
C			<1	as grown

III. EXPERIMENTAL DETAILS

A. Crystal growth and microstructuring by proton irradiation

Single crystals of $(FA)_2PF_6$ were grown by optimized electrocrystallization techniques[17] at $T=-30\,^{\circ}C$ at BIMF. Crystal structure was verified by x-ray structural analysis.[18] Energetic protons were utilized to introduce interruptions, or barriers, into the appropriate samples. For example, 25-MeV protons can traverse a range of 4.6 mm through a (fluoranthene)$_2PF_6$ single crystal. By using the appropriate radiation dose with a beam of such protons on a crystal of only 0.5 mm typical thickness, the resulting, essentially constant, energy loss dE/dl guarantees a statistically homogeneous radiation damage along a straight path through the entire sample. Three samples are compared in the current investigation, labeled as *A*, *B*, and *C* in the following (Table I): a homogeneously irradiated crystal *A*, a microstructured crystal *B*, and an as-grown crystal *C*. A high-energy proton beam ($E_P=25$ MeV, $I_P=0.1$ μA, exit diaphragm 2 mm) was used to damage the crystals locally ($t_P=0.75$ h). A brass grid with open and blocked spaces of 100-μm width each was used for the geometrical structuring [Fig. 2(a, b)]. The length of 2 mm of the brass stripes is sufficient to block the proton beam, if oriented parallel to the beam. This orientation was used for sample *B*. Figure 2(c) shows an optical photography of this sample: Areas shielded by the grid show up in black, those exposed to the proton irradiation show up

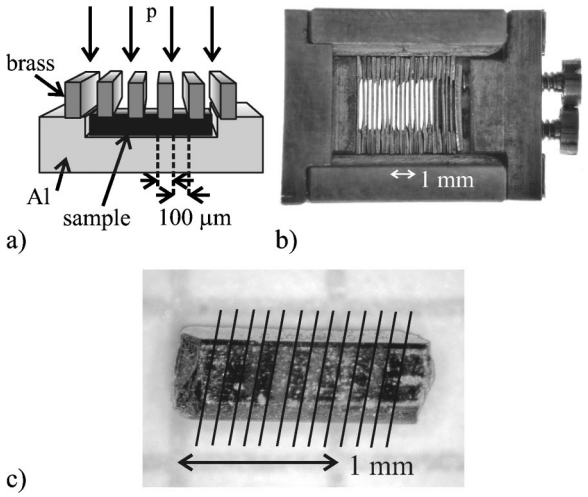

FIG. 2. Schematic representation of the configuration (a) and actual brass grid (b) used to microstructure the $(FA)_2PF_6$ single crystals by irradiation with high-energy protons. (c) Optical photography of a microstructured $(FA)_2PF_6$ single crystal. The solid lines are guides to the eye.

in gray. Solid lines are given in Fig. 2(c) as a guide to the eye. The 100-μm spacing can clearly be seen. For sample *A* this grid structure was inclined with respect to the proton beam and thus became transparent enough to allow a homogeneous irradiation of the sample. The irradiation characteristics were analyzed by simulations using the TRIM/SRIM 2000 simulation program.[19,20] These simulations show[1] that the proton beam is not broadened by more than about 2 μm during its path through the $(FA)_2PF_6$ crystal. The chemical and electronic nature of the damage induced in the organic conductor is unclear, however, and is thus a subject of particular interest in the current investigation.

B. Sample characterization

It has been shown earlier[21,22] that the quality of as-grown or aged $(FA)_2PF_6$ single crystals can be reasonably characterized by magnetic susceptibility and cw-ESR measurements. Whereas conduction electron paramagnetism clearly predominates at temperatures above the Peierls transition temperature ($T_P \approx 186$ K), low-temperature Curie paramagnetism reveals the concentration of unpaired defect spins. Depending on crystal growth conditions and sample aging, defect spin concentrations between 3×10^{-4} and 5×10^{-3} per formula unit were reported for $(FA)_2PF_6$ crystals.[21,22] The decomposition of the ESR susceptibility into a Curie-like contribution and a conduction electron contribution indicates a concentration of 5.8×10^{-4} Curie-like defects for the as-grown sample *C*, to be contrasted with the higher average concentration of 1.04×10^{-2} defects per formula unit of the microstructured sample *B* [Fig. 3(a)]. Nevertheless, this defect concentration is still only slightly higher than the defect concentration giving rise to the ESR linewidth minimum, as was observed for 1-MeV electron irradiated $(FA)_2PF_6$ crystals.[23] Additional information on the nature of the Curie-like paramagnetic defects is obtainable via low-temperature cw-ESR analysis.[21,22] The as-grown sample *C* in Fig. 3(b) shows the typical two-component ESR spectrum of a $(FA)_2PF_6$ single crystal of good quality.[21] In contrast, for the proton irradiated sample *B* [Fig. 3(c)], the broad line is buried under the huge intensity of the narrow delocalized-defect line. A rather large number of short chain segments must have been created by the irradiation (note the factor of 200 difference in vertical scale).[24] Proton irradiation must have been more harmful to the electronic properties of the $(FA)_2PF_6$ crystal than the simple Monte Carlo simulation[1,19] estimate of about 0.27×10^{-3} of removed target atoms. Assuming that no damage occurred to the protected areas, 2% of the FA dimers must be affected in the irradiated range, though counting only the magnetically detectable defects.

For comparison with earlier results of the anisotropy of the conduction electron spin diffusion constant $D_\parallel/D_\perp$ of $(FA)_2PF_6$ single crystals, we characterized the homogeneously irradiated as well as the geometrically microstructured crystals by static magnetic-field gradient spin-echo ESR also.[14] The average values thus obtained for samples *A* and *B* are compiled in Table II.[1] The parameter describing the diffusive echo attenuation for magnetic-field gradient perpendicular to the stacking direction, $D_\perp$, and thus presumably also the time constant $\tau_\perp$ for hopping of electron spins perpendicular to the stacking direction, is left unchanged by the irradiation. However, the average value of the diffusion constant parallel to the stacking direction, $\overline{D_\parallel}$, and correspondingly also the anisotropy $D_\parallel/D_\perp$, is reduced by about one order of magnitude compared to as-grown $(FA)_2PF_6$ crystals. This average parameter $\overline{D_\parallel}$ describing the spin-echo decay for magnetic-field gradient along the stacking axis will be compared with the spatial variation of the diffusion constant $D_\parallel$ below.

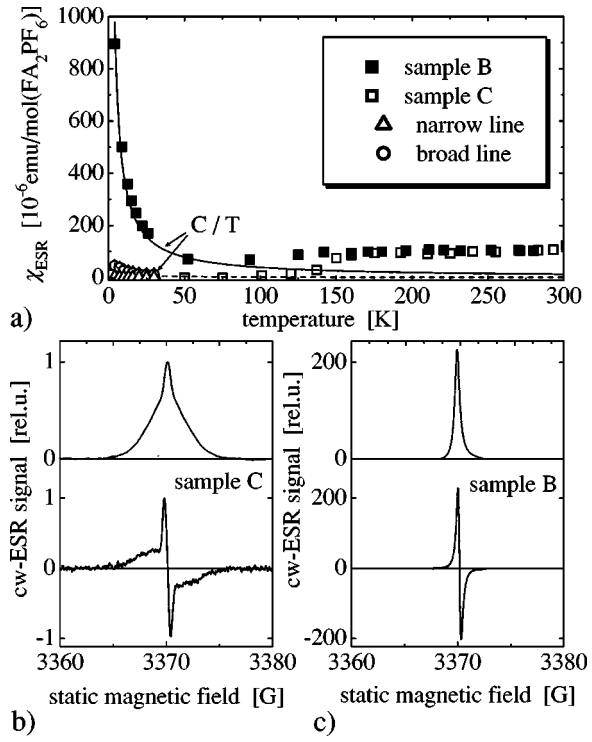

FIG. 3. cw-ESR characterization of $(FA)_2PF_6$ samples *B* and *C*. (a) Integral ESR susceptibility of microstructured (*B*) and as-grown (*C*) sample versus temperature at 9.5 GHz. (b), (c) At low temperature ($T=10$ K), two defect lines can be distinguished for sample *C*, in contrast to sample *B*. (Note $\times200$ change in vertical scales).

C. Pulsed electron spin resonance

Pulsed ESR was measured at $\nu_L=450$ MHz with a Tecmag APOLLO spectrometer and at $\nu_L=9.5$ GHz with a Bruker ELEXSYS ESP E580 *X*-band pulsed ESR spectrometer. Temperature was controlled with the help of Oxford Instruments He gas flow variable temperature cryostats. Static magnetic-field gradients of up to 0.2 T m^{-1} could be realized in the radiofrequency setup. The desired gradient

TABLE II. Diffusion constants of $(FA)_2PF_6$ samples ($T=250$ K).

Sample	$\overline{D_\parallel}$ (cm^2 s^{-1})	$\overline{D_\perp}$ (cm^2 s^{-1})	$\overline{D_\parallel}/\overline{D_\perp}$	$\tau_\perp$ (s)
A	0.081 ± 0.001	$(6.8\pm0.5)\times10^{-4}$	≈120	$\approx2.7\times10^{-11}$
B	0.071 ± 0.001	$(1.0\pm0.5)\times10^{-3}$	≈70	$\approx1.9\times10^{-11}$

was generated by two perpendicular home-developed gradient assemblies, an anti-Helmholtz coil pair for gradient along the main field direction ($G_z \equiv \partial H_z/\partial z$), and a second-order quadrupole system for the perpendicular direction $G_y \equiv \partial H_z/\partial y$. The direction of the gradient $G(\phi)$ in this spectrometer could be rotated electronically in the z-y plane, containing also the main field direction. For the *X*-band spectrometer, appropriate iron wedges installed between the pole caps of the electromagnet provided static gradient of up to 2.2 $\mathrm{T\,m^{-1}}$ in a fixed direction parallel to the main dc field ($G_z \equiv \partial H_z/\partial z$). To obtain the desired $G(\phi)$ rotations in that case, the sample had to be rotated around the appropriate axis. For calibration of the gradient $|G|$, the spectral width ΔB for a sample of known length L was analyzed as $|G| = \Delta B/L$. For 1D ESR projection ''image,'' the irradiated sample should be oriented ideally with the conduction direction along the gradient, i.e., with the damaged planes perpendicular to the gradient. For two-dimensional ESR imaging of the irradiated crystals, the filtered projection reconstruction technique was applied.[25] However, the polar grid was projected on a Cartesian lattice for further analysis, a procedure requiring interpolation. For further experimental details we refer to Ref. 1. Individual pixel (i,j) information was extracted by fitting the equation

$$\frac{M_{ij}(2\tau)}{M_{ij}(0)} = (1-a)\exp\left\{-\frac{2\tau}{T_{2,del}} - \frac{2}{3}\gamma^2 G^2 D \tau^3\right\} + a\exp\left\{-\frac{2\tau}{T_{2,loc}}\right\}. \quad (1)$$

Thus a portion ''a'' of localized spins with possibly different relaxation time $T_{2,loc}$ in addition to the ''free'' spins with diffusion constant D and relaxation time $T_{2,del}$ was considered. Expression (1) is a reasonable model representation of the intensity of the spectral data points, used as ''1D pixels,'' in a 1D projection scheme. It should be considered at this stage only as a convenient *ad hoc* approximation for the signal intensity of pixels in a 2D back projection reconstruction image. This point will be discussed further in Secs. IV and V.

IV. RESULTS AND ANALYSIS OF ELECTRON SPIN IMAGING EXPERIMENTS

A. Homogeneously irradiated crystals

The *average* diffusion constant for the homogeneously irradiated sample *A* (Table II), derived by SGSE-ESR analysis without spatial resolution, is $D_\parallel = (0.081 \pm 0.001)\ \mathrm{cm^2\,s^{-1}}$. This value is about one order of magnitude smaller than the electron spin diffusion constant $D_\parallel$ of as-grown $(FA)_2PF_6$ single crystals at $T \approx 250$ K, which ranges between 2 $\mathrm{cm^2\,s^{-1}}$ and 0.2 $\mathrm{cm^2\,s^{-1}}$, depending on crystal quality.[5,14,15] Thus, within a time interval of $\tau \cong 5\ \mu$s (the lower limit of T_2), the ESR spin echo decays only negligibly (by about 0.2%) in a magnetic-field gradient of $G = 0.03\ \mathrm{T\,m^{-1}}$ due to the diffusive motion of the spins. On the other hand, this small diffusion constant is favorable for spatial resolution, because we estimate via $\overline{(\delta r_\parallel)^2} = 2D_\parallel \tau$ a typical smearing of merely $\delta r_\parallel \cong 9\ \mu$m along the conducting direction (and only about 0.8 μm in the perpendicular direction). Thus, by acquiring a series of low field gradient 2D PR images of the homogeneously irradiated crystal *A* over an extended pulse separation τ range, and fitting the series of images, pixel by pixel, to the appropriate relaxation function, the distribution of transverse relaxation times T_2 in the sample can be obtained (Fig. 4). Sample *A* had its smallest dimension in the unresolved direction, thus information concerning a voxel (volume element) volume of $(28\ \mu\mathrm{m})^2 \times 350\ \mu$m (Table I) is presented in Fig. 4.

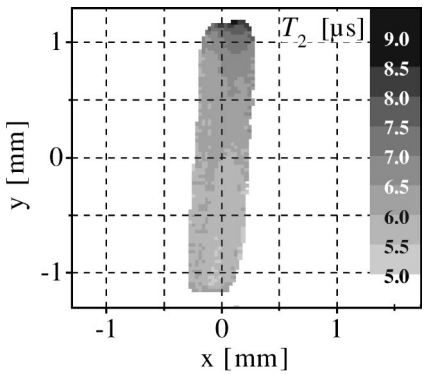

FIG. 4. Two-dimensional spatially resolved distribution of transverse relaxation time T_2 of the homogeneously irradiated sample *A* (Table I). [$\nu_L = 450$ MHz, $G = 0.030\ \mathrm{T\,m^{-1}}$, $T = 250$ K, pixel size $(28\ \mu\mathrm{m})^2$].

No substantial variation is derived for $D_\perp$, on the other hand. These observations are borne out by the spatial resolution of $D_\parallel(r)$ that was achieved in a deliberately microstructured $(FA)_2PF_6$ crystal, as presented for sample *B* in the following.

B. Microstructured crystal

Table II shows that the average diffusion constants $\overline{D_\parallel}$ and $\overline{D_\perp}$ of the microstructured crystal *B* do not differ substantially from those of the homogeneously irradiated crystal *A*. Thus it is evident that the damaged regions, with slower spin-echo decay, predominate in the integral SGSE-ESR signal. Obviously, a spatially resolved ESR data acquisition is called for. The only *X*-band ESR imaging option at our disposal currently is a variant of the 2D projection-reconstruction (PR) magnetic resonance imaging scheme, in which data are acquired while rotating the direction of the field gradient $G(\theta)$ with respect to the coordinates of the imaged sample. The implied assumption in PR is that the ESR signal *intensity* from a given pixel is independent of θ. It is *a priori* not guaranteed that the PR method will provide numerically reliable contrast images for samples where the echo signal is only locally damped by rapid *and* anisotropic diffusion—as is expected for the undamaged regions in sample *B*. Thus, as a first step, we will treat only one-dimensional projections, in which data are acquired for single fixed gradient orientation along a desirable direction in the sample. As already mentioned at the end of Sec. III, for gradient in the direction of the conduction chains the

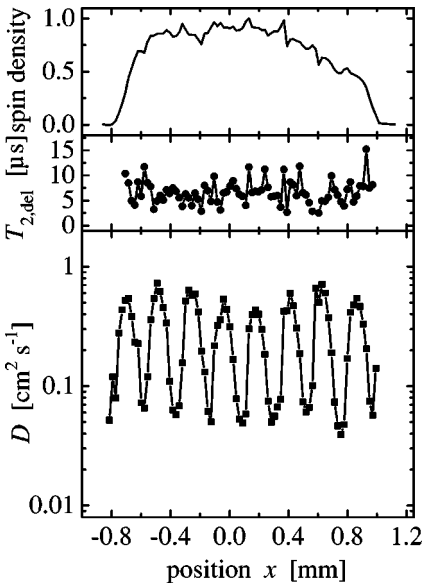

FIG. 5. One-dimensional resolved distribution of spin density, transverse relaxation time $T_{2,del}$, and diffusion constant $D_{\parallel}$ of microstructured sample *B*. ($T=250$ K, $\nu_L=9.5$ GHz, $G=0.81$ T m^{-1}, 1D projection onto stacking direction).

numerical intensity of the signal along such projection is reasonably well represented by Eq. (1).

1. One dimensional projection

The data in Figs. 5 and 6 were fitted in terms of the four physical parameters contained in the two-component model represented by Eq. (1). Figure 5 shows the total one-dimensional distribution of spin density $\rho(x)$, the transverse relaxation time $T_{2,del}(x)$, and diffusion constant $D_{\parallel,del}(x)$ of the delocalized fraction, all three as functions of the position x along the conduction chains in the crystal. The field gradient was oriented in this case perpendicular to the irradiated planar regions (which means perpendicular to the direction of the proton beam used to damage the crystal), which was not exactly parallel to the stacking axis—see Fig. 2(c). Figure 6, on the other hand, shows the distribution of

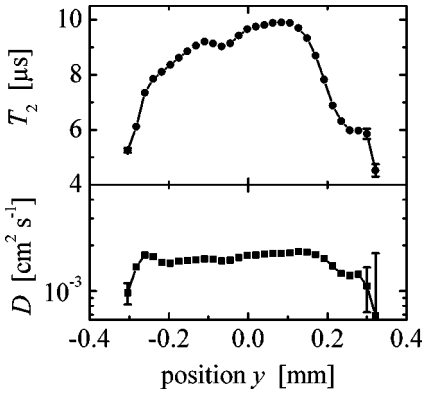

FIG. 6. One-dimensional resolved distribution of transverse relaxation time T_2 and diffusion constant $D_{\perp}$ of microstructured sample *B*. ($T=250$ K, $\nu_L=9.5$ GHz, $G=0.33$ T m^{-1}, projected along stacking axis).

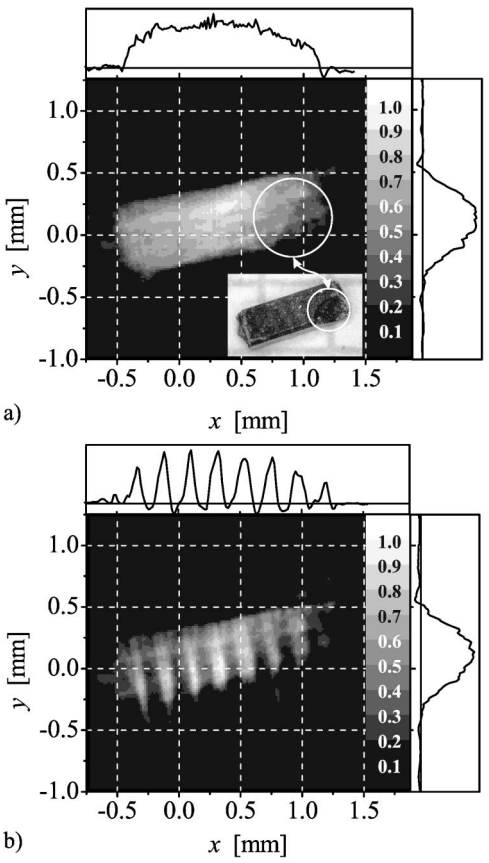

FIG. 7. Two-dimensional spin density projection of the microstructured sample *B* and its one-dimensional projections on the x and y axes ($\nu_L=9.5$ GHz, $G=0.81$ T m^{-1}, $T=250$ K). Pixel size (16 μm)^2. (a) $\tau=0.5$ μs, the optical photograph (inset) shows the broken corner (white circle). (b) $\tau=1.5$ μs, regions with reduced spin diffusion give rise to the bright stripes visible in this projection.

$T_2(y)$ and $D(y)$ plotted in the perpendicular orientation along the shorter dimension of the sample labeled ''y.'' For these plots, the gradient was applied as nearly as possible perpendicular to the conduction axis and thus the signals are projected along the crystal needle axis. Both data sets were acquired at *X*-band frequency, at $T=250$ K, and applying a gradient of $G=0.81$ T m^{-1}. The total spin density plot $\rho(x)$ is essentially constant—except for the effect of the small broken edge represented also optically in Fig. 7. In the metallic phase of $(FA)_2PF_6$ at 250 K, the proton irradiation thus has no significant effect on the absolute value of the total local paramagnetic susceptibility $\chi(r)$, as could be surmised already from inspection of the integral data in Fig. 3. The weak variation of $T_2(x)$ visible in Fig. 5 is similar to the behavior seen in Fig. 4 for sample *A*. Even more drastic but not unfamiliar[11] variation of $T_2(y)$ was observed for the orientation perpendicular to the needle axis (Fig. 6). The decrease of $T_2(y)$ and $D(y)$ at both outer sides of crystal *B* (Fig. 6)—outside of $y=\pm 0.2$ mm, i.e., *on the surface* along the needle axis—points to a comparatively large concentration of localized defects (larger than 1%) in these surface regions. This is not unexpected in view of the average concentration of 1% per formula unit reported in Sec. III B for the whole crystal *B*.

The most dramatic result is the very large periodic variation of the diffusion constant $D(x)$ with position x, with a ratio exceeding one order of magnitude (Fig. 5). The maxima of $D_{max}=(0.6\pm0.2)$ cm^2 s^{-1} are observed in the shielded, thus undamaged, regions of crystal *B*. This value is within the range typically observed for as-grown $(FA)_2PF_6$ crystals. On the other hand, the minima of $D_{min}=(0.055\pm0.015)$ cm^2 s^{-1} are found in the regions that were exposed to the beam, thus damaged by proton irradiation. These lower absolute values compare reasonably with the values derived for the homogeneously irradiated crystal *A*. Because of the much slower diffusion, the signal from these regions dominates in the integral derivation of the apparent total diffusion constant $D_\parallel$ of sample *B* as listed in Table II. The damage in $(FA)_2PF_6$ crystals created by the proton irradiation reduces thus the conduction electron spin diffusion constant D (presumably their self-diffusion coefficient) *locally and drastically*. Our attempt of a two-dimensional imaging of these distributions is presented in the following section.

2. Two-dimensional images

Figure 7 shows two examples of two-dimensional images of the microstructured crystal *B*, obtained at $T=250$ K with a 9.5-GHz ESR spectrometer. Standard 2D PR was utilized for both with $|G(\theta)|=0.81$ T m^{-1}. A nominal 2D resolution of $(16\ \mu m)^2$ is obtained, with a voxel size of $(16\ \mu m)^2\times550\ \mu m$, the third dimension being determined by the sample thickness. For convenience in the following, we define θ as the angle between $\vec{G}$ and the conducting chains. Figure 7(a) was acquired with rf pulse separation $\tau=0.5\ \mu s$ and Fig. 7(b) with $\tau=1.5\ \mu s$.

We treat first Fig. 7(a). It follows from Eq. (1) that for a sufficiently short τ, i.e., for

$$\tau \ll T_2, \{\gamma^2 G^2(\theta)\cos^2(\theta) D\}^{-1/3}, \tag{2}$$

the signal intensity from each voxel depends mostly on the local spin density. This is essentially the condition under which the image in Fig. 7(a) was acquired. Indeed it can be verified that for this short echo time, even in regions with D_{max} (Sec. IV B 1), and for $\theta\cong0$, only 10% echo attenuation is realized. The total diffusion attenuation from such voxels is even further moderated by the many contributions from projections in which $\vec{G}$ points away from $\theta\cong0$. It is therefore not surprising that Fig. 7(a) exhibits a rather uniform signal intensity distribution. This distribution must be reflecting the existence of essentially uniform spin-density distribution in the microstructured sample. Comparison of the PR image with the photographic picture [inset in Fig. 7(a)] verifies that the PR procedures used preserve indeed the *metrics* of the imaged sample, and the linearity of the imaging procedure can be judged also by the fact that the broken edge of the crystal—inset to Fig. 7(a)—can be actually recognized in the ESR "spin density" image. Finally, Fig. 7(a) supports the conclusion from Secs. IV A and IV B 1: The ESR susceptibility $\chi(r)$—dubbed "spin density" for simplicity, but somewhat oversimplifying—in the metallic phase of the microstructured sample *B* is not modulated significantly by the proton beam irradiation. Note, however, that this may be true only for the presently applied radiation dose, which created just an average defect concentration of 1% per formula unit, leaving the cw-ESR linewidth in the range of its defect concentration dependent minimum.

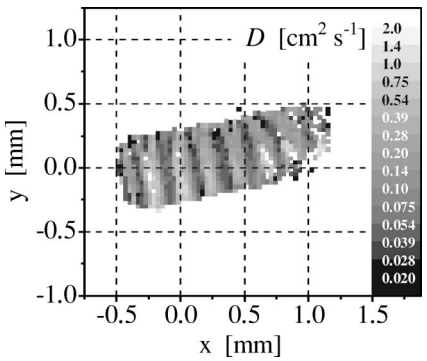

FIG. 8. Two-dimensional spatially resolved map of the diffusion constant D for microstructured sample *B*, Pixel size $(32\ \mu m)^2$, based on fit of Eq. (1).

We turn now to Fig. 7(b), acquired with $\tau=1.5\ \mu s$, i.e., under circumstances for which the inequality (2) is rather compromised. Note first that for echo time (TE) of 3 μs, values of $D_{max}\simeq0.6$ cm^2 s^{-1} existing in undamaged regions in the sample imply already rms diffusive migration $\delta r_\parallel=19\ \mu m$. This migration exceeds the pixel dimension along the conducting chains and therefore, in principle, would constitute a practical resolution limit along that direction. The most significant change caused by increasing τ can be clearly seen visually. Whereas a rather uniform signal density distribution [Fig. 7(a)] is obtained for $2\tau=1\ \mu s$, Fig. 7(b), on the other hand, shows nicely the 100 μm alternating bright and dark stripes impressed by the proton irradiation. The damaged regions, with a small diffusion constant, appear as bright stripes while undamaged regions with a high diffusion constant are to a large extend wiped out in Fig. 7(b). This dramatic dependence of pixel intensities on TE is of course a direct result of the τ^3 term included in the *exponent* in the diffusive echo attenuation expression (1).

As alluded to in Sec. III C, with τ values for which relation (2) is not satisfied, experimental pixel intensities in a 2D PR image are not represented analytically by Eq. (1). However, encouraged by the results shown in Fig. 7 and assuming the systematic errors involved are well behaving, one is tempted to try and analyze the τ dependence of pixel intensities in 2D PR images in terms of the two component model of Eq. (1). To this end, 2D PR images of the microstructured crystal were acquired over an extended τ range, $0.3\ \mu s\leqslant\tau\leqslant10.2\ \mu s$. Individual pixels—now enlarged to $(32\ \mu m)^2\times550\ \mu m$ to improve the signal-to-noise ratio (S/N)—were then analyzed on the basis of Eq. (1). This way, two-dimensional maps of the fraction "a" of localized spins[1] and of the effective diffusion constant "D" of the "free" spins (Fig. 8) were generated. The successful microstructuring of crystal *B* can thus very clearly be observed: The modulation of the diffusion constant by at least one order of magnitude, with its maxima in the undamaged regions, and the complementary variation of the localized spin portion a, with the maxima in the irradiated parts of the crystal. It is indeed

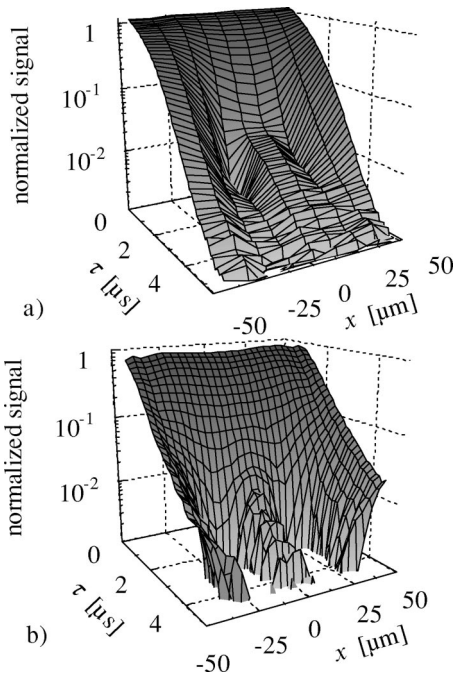

FIG. 9. One-dimensional projection of the magnetization for a single nonirradiated 100-μm region in the microstructured sample *B* (projected onto the conducting direction, only the positive part of the ''real'' signal shown). (a) experiment, (b) random-walk simulation.

gratifying to note that the *ad hoc* derived values of *D* in Fig. 8 are essentially in agreement with the *D* values derived by fitting the ''analytic model'' of Eq. (1) to the 1D projection data. As was discussed already, based on the one-dimensional projections (Sec. IV B 1) a comparatively large fraction of defect spins is also imaged along the long sides of the $(FA)_2PF_6$ crystal. Note that in some of the irradiated regions, the fraction *a* reaches up to 100%. However, it is not yet clear if this observation is not an artifact caused by the systematic errors mentioned earlier.

C. Coherence phenomena of spin diffusion

Three-dimensional imaging of $(FA)_2PF_6$ crystals showed earlier[2,11] that free diffusive motion of conduction electron spins from one end of the crystal to the other may be possible in high-quality crystals. Therefore, the steep geometric steplike change in density of localized defects and in the diffusion constant *D*, realized by proton beam microstructuring of crystal *B*, opens the possibility to observe the diffusive dynamics of conduction electron spins that are locked up between ''impermeable'' walls with a 100-μm separation. Remembering the pessimistic view of Fig. 1, however, we should note that not all walls can be perfect.

Figure 9(a) shows an example of echo signals in one of the 100-μm conductive blocks created in crystal *B* by proton irradiation. Shown is a 1D projection of the signal onto the conducting direction labeled *x* in the figure, along the proton beam direction. In order to profit from the logarithmic scale, only the positive values of the real part of the projected signal are plotted in Figs. 9(a), 9(b), and 10. The qualitative

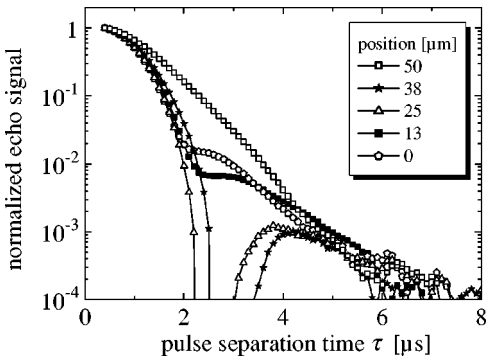

FIG. 10. Measured echo signal (1D projection) versus pulse separation τ at five different positions within one half of a nonirradiated 100-μm block (sample *B*).

agreement between the experimental observation [Fig. 9(a) and 10] and the results of a random walk simulation [Fig. 9(b)][1] is striking. The coherence phenomena are clearly demonstrated for the diffusion process. At short waiting times, magnetization diffuses with the square root of time back and forth between the reflecting walls, giving rise to interference between forward and backward diffusing magnetizations. Thus for fixed channel length, some kind of ''standing wave'' behavior results, exponentially damped, but observable nevertheless. It should be kept in mind that a 1D projection of the magnetization (resolved perpendicular to the proton beam direction, along the conducting chain) is calculated and analyzed here, thus the nonideal ''walls'' give rise to some additional smearing of the calculated structures. But the signal minima for $\tau \approx 2.5$ μs can clearly be observed, a proof of the parallelism of the walls at least for this individual block.

V. DISCUSSION

Due to their weak spin-orbit coupling and one-dimensionally restricted motion, the conduction electron spins in arene radical cation salts such as $(FA)_2PF_6$ exhibit an extremely narrow ESR line of 15-mG peak to peak or below, and transversal relaxation times T_2 of 5 μs or above at temperatures between room temperature and their Peierls transition temperature. Thus these systems are useful as model systems for a detailed analysis based on pulsed ESR techniques. ESR properties are extremely sensitive to the interaction of the delocalized (conduction) electron spins and localized defect spins built in into the one-dimensional arene stacks. Exchange interaction between both types of spins modulates their dipolar interaction and gives rise to characteristic temperature dependences of absolute value and anisotropies of longitudinal (T_1) and transverse (T_2) relaxation times, most pronounced around and below the Peierls transition temperature, where the conduction electron susceptibility varies drastically due to the opening of the low-temperature energy gap.[21,22] ESR linewidth and $1/T_2$ relaxation rates depend in a peculiar way on the concentration of paramagnetic defects due to a bottleneck situation of the relaxation to the lattice. Thus with increasing concentration of paramagnetic defects from the lowest achieved values

("optimal" defect concentration) of typically less than 10^{-4} defects per formula unit, the observed linewidth and $1/T_2$ rate decrease down to a minimum in the 0.1–0.5 % defect concentration range, and increase again dramatically only for relative concentrations well above 1%. The diffusion constant $D_\parallel$ in optimal samples is in the 2-4 $cm^2\,s^{-1}$ range, and the value decreases monotonically with increasing defect concentration. The influence of defect concentration was systematically studied also for electron beam irradiated $(FA)_2PF_6$ crystals in the past.[23] In principle, the same phenomena is "exploited" presently with proton irradiated $(FA)_2PF_6$ crystals. Pertaining to the present study, the analysis of our RF 2D PR data (Fig. 4) indicates the existence of a distribution of relaxation times in the irradiated crystals, with $T_2 \approx 9$ μs at the upper very end (Fig. 4), about a factor of 2 longer than at the opposite end. It should be mentioned that the cw-ESR linewidth decreased a little upon irradiation for sample *A*, indicating that its defect concentration was not yet raised substantially above the characteristic concentration for the linewidth minimum[23] in $(FA)_2PF_6$. It may be also noted that an even larger variation of the transverse relaxation times T_2 has been demonstrated recently for an as-grown $(FA)_2PF_6$ crystal perpendicular to the stacking direction,[11] which could be correlated with a comparable variation of the longitudinal relaxation time T_1. Thus, while defect content may influence the electron spin relaxation times of $(FA)_2PF_6$ crystals generally, no clear correlation has been demonstrated or found in the current investigation between proton irradiation damage and transverse electron-spin relaxation.

The influence of homogeneous irradiation with protons is much more clearly seen in the reduction of the diffusion constant for motion along the highly conducting FA-stacking direction, $D_\parallel$ (Table II). From the cw-ESR analysis it is concluded that the present "as-grown" samples contained about 6×10^{-4} Curie-like defects per formula unit. With this slightly higher than optimal concentration, a somewhat reduced diffusion along the stacks $D_\parallel$ is usually observed, in the range of 0.2-1.0 $cm^2\,s^{-1}$. Indeed, we find $D_\parallel \simeq 0.6$ $cm^2\,s^{-1}$ in undamaged regions of sample *B*. After irradiation, the cw-ESR derived Curie defect concentration is raised to about 1% per formula unit on the average for the microstructured crystal, probably even up to a factor 2 higher in the damaged regions. As determined from the 1D projection analysis (Sec. IV B 1), this 1–2 % defect density reduces the diffusion constant $D_\parallel$ in damaged regions already by a factor of 10 in comparison with as-grown crystals of comparable quality. However, both $D_\perp$ in the microstructured sample *B* and $D_\perp$ in the homogeneously irradiated sample *A* are not varied outside the typical distribution of the values observed for their counterpart in as-grown crystals. Thus the intrastack defects created by proton radiation damage do not increase the perpendicular hopping probability.

It should be noted that the nature of proton-induced damage responsible for the observed reduction of both the ESR linewidth and $D_\parallel$ is not clear at present. The estimated concentration of paramagnetic "localized" (i.e., Curie-like) defects in the irradiated crystals, based on the cw-ESR analysis and the measured diffusion coefficients, is ~30–60 times larger than the estimated concentration of atomic displacements created by the proton irradiation. One may consider the possibility that each displacement creates several paramagnetic defects around it. It is also feasible to consider ionization processes. The number of ionizing collisions of the traversing proton in solid matter is several order of magnitudes larger than the related number of atomic displacements. Even if only a small fraction of these ionizations remain unrelaxed, it may provide the required paramagnetic defects.

Both the 1D projection data and the 2D PR imaging data reflect clearly the microstructured damage induced by the proton irradiation. Under the timing constraints imposed by T_1 and T_2, it is instrumentally much easier to implement a PR imaging than a Fourier imaging scheme, and in fact the latter is presently not available in our lab. It is thus of interest to examine the validity of the 2D PR imaging scheme in the present case of anisotropic mobility of the imaged spins. It was realized earlier[12,26] that, unlike the case with Fourier-imaging or a well-selected 1D projection experiment, the anisotropic diffusion leads inherently to systematic errors in PR images. However, comparing the metrics and the value of the relevant physical parameters as derived independently from our 1D projection and the 2D PR images, no significant numerical differences can be discerned, at least under the current range of experimental conditions (bandwidth, gradients, pulse separation, and S/N). Performing recently a series of numerical simulations of our 2D PR experiment, it was verified indeed that a reasonable 2D spatial mapping of D is to be expected by using the above procedure, although serious systematic error artifacts can occur in the spin-density map of the localized fraction. We conclude that the "maps" shown in Figs. 7(a) and 8 constitute a reliable *ad hoc* representation of the spatial distribution of the total spin density $\rho_{tot}(x,y)$ and the diffusion of the delocalized fraction $D_{\parallel,\,del}(x,y)$, respectively. Thus, the modulation of the diffusion by one order of magnitude, displayed already in the 1D distribution (Fig. 5), is seen clearly in Fig. 8 to be evenly distributed along the "y" direction, i.e., along the ~550-μm path of the proton beam generating the damaged 100-μm-thick planar regions through the crystal. It was previously shown for other radical-cation salt systems that the measured spin diffusion can be identified with the self-diffusion coefficient of the conduction electrons.[13] It is thus concluded that the conduction electron mobility is imaged in Fig. 8, and this mobility is modulated by more than one order of magnitude by proton irradiation. This observation opens up the way to deliberate preplanned geometric manipulation of mobility distribution in related arene radical cation salts.

According to our simulations, proton irradiation can be microstructured to within about 2 μm along the beam trajectory, assuming perfect mechanical dimension of the mask assembly. As can be actually seen in Fig. 2(b), our current realization of the grid mask is less than perfect, causing additional loss of resolution in the generated damaged pattern. Nevertheless, we could use the conducting blocks of nominal 100-μm thickness, bracketed between 100-μm-thick barriers of low mobility and high concentration of localized (but in-

teracting) defects, to analyze the time dependence of the electron spin magnetization following a pulsed excitation in the static magnetic-field gradient. The time and spatially varying echo signal amplitudes compare indeed reasonably with simulations that used the known diffusive motion and assumed a complete reflection from perfect ''walls'' of the 100-μm block (Figs. 9 and 10).

VI. CONCLUDING REMARKS

Using two-dimensional projection reconstruction algorithms with pulsed *X*-band ESR spectrometer, various ESR accessible properties were investigated presently in the quasi-one-dimensional organic conductor $(\text{fluoranthene})_2\text{PF}_6$. In particular, we derived the spatial distribution of spin susceptibility, transverse relaxation rate, diffusion constant, and portion of nondiffusing (or weakly diffusing) spins in the metallic phase of $(\text{FA})_2\text{PF}_6$, and the influence of proton induced radiation damage on these parameters. A modern *X*-band pulse spectrometer can generate very fast pulse sequences, with pulse separations as short as 100 ns, and large magnetic-field gradients become tolerable due to the large bandwidth of about 200 MHz available in such a spectrometer. These attributes appear to enable the implementation of ESR imaging schemes also for samples with larger diffusion coefficients, exceeding the presently investigated maximal value of 0.6 $\text{cm}^2\,\text{s}^{-1}$. Eventually, the anticipated improved S/N of these modern spectrometers will enable the investigation of induced carrier motion—e.g., externally driven currents—as well, as long as the electrical conductivity and the sample thickness are small enough so as not to create skin-effect problems.

In this investigation, modification of the properties of two $(\text{FA})_2\text{PF}_6$ crystals by irradiation with high-energy (25 MeV) protons has been realized. Both homogeneous distribution of defects and preplanned microstructured square-wave-shape distribution of defects with a period of 100 μm and about 2-μm resolution were demonstrated. A reduction of the diffusion constant (supposed to reflect the mobility) by a factor of 10 is achieved even by the moderate dose of 5.4×10^{16} 25-MeV protons per cm^2, paving the way to an arbitrary tailoring of mobility distributions in this and related arene cation salts. The moderate radiation damage raised the concentration of Curie-like defects—from an initial value of 6×10^{-4}—just enough to enter the 1% range. This, in turn, results with a rather intense and narrow cw-ESR line even in the 10-K range, far below the Peierls-transition temperature of typical arene radical cation salt crystals. While interesting on its own merit,[21,22] the intense low-temperature narrow-line ESR signal has also promising potential for instrumentation applications.

ACKNOWLEDGMENTS

We are indebted to G. Alexandrowicz, T. Tashma, A. Feintuch, and J. U. von Schütz for discussions and B. Pongs for experimental contributions. We thank P. Höfer and Bruker/Karlsruhe for the opportunity to perform early pulsed ESR measurements at 10 GHz. N.K. thanks the Deutsche Forschungsgemeinschaft/SFB 195 (Universität Karlsruhe) for support. This project was supported by the DFG (Do 181/10).

*On leave from Racah Institute of Physics, Hebrew University, Jerusalem 91904, Israel.

[1] T. Wokrina, Ph.D. thesis, Universität Karlsruhe, Germany, 2002.
[2] G. Alexandrowicz, T. Tashma, A. Feintuch, A. Grayevsky, E. Dormann, and N. Kaplan, Phys. Rev. Lett. **84**, 2973 (2000).
[3] G.G. Maresch, A. Grupp, M. Mehring, J.U. von Schütz, and H.C. Wolf, J. Phys. (Paris) **46**, 461 (1985).
[4] G.G. Maresch, Ph.D. thesis, Universität Stuttgart, Germany, 1987.
[5] M. Mehring, in *Low-Dimensional Conductors and Superconductors*, edited by D. Jerome and L. G. Caron (Plenum, New York, 1987), p. 185.
[6] G. Sachs, W. Stöcklein, B. Bail, E. Dormann, and M. Schwoerer, Chem. Phys. Lett. **89**, 179 (1982).
[7] H.C. Torrey, Phys. Rev. **104**, 563 (1956).
[8] J.E. Tanner and E.O. Stejskal, J. Chem. Phys. **49**, 1768 (1968).
[9] N. Kaplan, E. Dormann, R. Ruf, A. Coy, and P.T. Callaghan, Phys. Rev. B **52**, 16 385 (1995).
[10] R. Ruf, N. Kaplan, and E. Dormann, Phys. Rev. Lett. **74**, 2122 (1995); **75**, 1237 (1995); **76**, 334 (1996).
[11] T. Tashma, A. Feintuch, A. Grayevsky, J. Gmeiner, A. Gabay, E. Dormann, and N. Kaplan, Synth. Met. **132**, 161 (2003).
[12] A. Feintuch, T. Tashma, A. Grayevsky, J. Gmeiner, E. Dormann, and N. Kaplan, J. Magn. Reson. **157**, 69 (2002).
[13] T. Tashma, G. Alexandrowicz, N. Kaplan, E. Dormann, A. Grayevsky, and A. Gabay, Synth. Met. **106**, 151 (1999).
[14] T. Wokrina, E. Dormann, and N. Kaplan, Europhys. Lett. **49**, 244 (2000).
[15] T. Wokrina, E. Dormann, and J. Gmeiner, Synth. Met. **120**, 847 (2001).
[16] T. Wokrina, E. Dormann, and N. Kaplan, Phys. Rev. B **54**, 10 492 (1996).
[17] C. Kröhnke, V. Enkelmann, and G. Wegner, Angew. Chem. **92**, 941 (1980).
[18] V. Enkelmann, Adv. Chem. Ser. **217**, 177 (1988); C. Buschhaus (private communication).
[19] http://www.srim.org, Version 2000.40.
[20] J.P. Biersack and L.G. Haggmark, Nucl. Instrum. Methods **174**, 257 (1980).
[21] G. Sachs and E. Dormann, Synth. Met. **25**, 157 (1988).
[22] E. Dormann and G. Sachs, Ber. Bunsenges. Phys. Chem. **91**, 879 (1987).
[23] J.M. Delrieu, M. Beguin, and M. Sanquer, Synth. Met. **19**, 361 (1987).
[24] I. Baldea, H. Köppel, and L.S. Cederbaum, J. Phys. Soc. Jpn. **68**, 1954 (1999).
[25] P.T. Callaghan, *Principles of Nuclear Magnetic Resonance Microscopy* (Oxford Science Publications, Oxford, 1995).
[26] A. Feintuch, G. Alexandrowicz, T. Tashma, H. Boasson, A. Grayevsky, and N. Kaplan, J. Magn. Reson. **142**, 382 (2000).